Check for updates

Effect of Subsurface Microstructures on Adhesion of Highly Confined Elastic Films

Manar Samri
INM—Leibniz Institute for New Materials,
Saarbrücken 66123, Germany;
Department of Materials Science and Engineering,
Saarbrücken 66123, Germany
e-mail: manar.samri@leibniz-inm.de

Attila Kossa
Department of Applied Mechanics,
Faculty of Mechanical Engineering,
Budapest University of Technology and Economics,
Budapest 1111, Hungary
e-mail: kossa@mm.bme.hu

René Hensel[1]
INM—Leibniz Institute for New Materials,
Saarbrücken 66123, Germany
e-mail: rene.hensel@leibniz-inm.de

Polymer adhesive films sandwiched between two rigid solids are a common bonding strategy. The mechanics and consequently the adhesion of such geometrically confined films depend mainly on their thickness, Young's modulus, and the Poisson's ratio of the material. In this work, we explore the effect of a micropatterned subsurface embedded into the adhesive layer. We compare experiments with three-dimensional numerical simulations to evaluate the impact of the microstructure on the contact stiffness and effective modulus. The results are used to extend a previously proposed size scaling argument on adhesion from incompressible to slightly compressible films to account for the silicone used in our study with a Poisson's ratio of 0.495. In addition, interfacial stress distributions between the elastic film and the glass disc are obtained from plane strain simulations to evaluate characteristic adhesion failures such as edge cracks and cavitation. Overall, the micropatterned subsurface has a large impact on the contact stiffness, the interfacial stress distribution, and the detachment behavior; however, the adhesion performance is only slightly improved in comparison to a non-patterned subsurface. [DOI: 10.1115/1.4049182]

Keywords: computational mechanics, micromechanics, adhesion, bioinspiration

1 Introduction

Polymer adhesive films are widely used for the assembly of components in several industries. Such films are usually thin which means that the thickness is much smaller than their lateral dimensions. When located in between two nominal flat, rigid solids, and a force applied normal to the film, the adhesion strength scales with the film thickness, $h^{-0.5}$, as described by Kendall in 1971 [1]. In strict terms, this scaling argument is only correct for incompressible films with a Poisson's ratio of 0.5, i.e., the volume remains constant during normal pulling. However, the adhesion of the film to the solids hinders lateral deformations, which results in a virtually stiffer film with a larger effective Young's modulus [2] and a higher contact stiffness [3]. The phenomenon is referred to as the confinement effect, which supports adhesion [1–3].

Compressible materials with Poisson's ratio $\nu < 0.5$ undergo volumetric deformations to overcome lateral distortions due to the confinement [4]. In fact, the confinement effect is neglectable for $\nu = 0$. We have recently demonstrated that even for materials with very low compressibility ($0.48 < \nu < 0.5$), the effective modulus varies dramatically in terms of ν [2]. For instance, the effective modulus for a highly confined film with $\nu = 0.48$ can be more than three orders of magnitude smaller than for a similar film made from an incompressible material with $\nu = 0.5$. This observation is of particular relevance, since elastomers that are often assumed to be incompressible are usually slightly compressible. For example, silicone elastomers have Poisson's ratios of about 0.495 [5]. Although such a deviation from the theoretical limit of 0.5 is small, its impact on the confinement effect can be tremendous, as demonstrated in previous theoretical analyses [2,6].

In addition to the contact stiffness and effective Young's modulus, the stress distribution along the contact interface and, therefore, the detachment mechanism vary with the degree of confinement [7]. A punch in contact with an unconfined film typically leads to a dominating edge stress singularity, which induces detachment via edge cracks. When the same punch is in contact with a highly confined film, the intensity of the edge singularity is reduced and the stress at the center of the contact is enhanced [2,8]. This then results in detachment via cavitation or finger instabilities [9–11]. It should be noted that the interfacial stress distribution is sensitive to the Poisson's ratio as well [2].

In the present work, we report on the adhesion of confined elastic films in the presence of a stiffer subsurface microstructure and compare it to a non-patterned subsurface. Experimental stiffnesses and effective moduli of the adhesives are compared with three-dimensional (3D) numerical simulations. The adhesion results are compared with a universal scaling argument, which is extended to compressible, linear elastic films. Finally, stress distributions at the adhesive interface are determined from plane strain simulations and compared to characteristic detachment patterns recorded at pull-off. The effect of the Poisson's ratio and the radius of the glass disc are also investigated and evaluated.

2 Materials and Methods

2.1 Silicone Films With Micropatterned Epoxy Subsurfaces. Smooth silicone films with micropatterned epoxy subsurfaces were prepared as follows. Epoxy micropillar arrays were replicated from silicon master templates (TU Dresden, Germany) using molds made from Elastosil M4601 (Wacker Chemie AG, München, Germany). The two-component Elastosil was mixed in a 9:1 ratio at 1200 rpm and degassed at 1 mbar for 90 s using a SpeedMixer (DAC600.2 VAC-P; Hauschild & Co. KG, Hamm, Germany). The pre-polymer mixture was poured onto the silicon master and cured at 75 °C in an oven for 2 h. Subsequently, the Elastosil mold was used to fabricate the epoxy micropillar arrays (Yachtcare Epoxy BK, Soloplast Vosschemie, Germany). The two-component epoxy was mixed in a 10:6 ratio at 2350 rpm and degassed at 1 mbar for 3 min using a SpeedMixer. The epoxy pre-polymer mixture was poured onto the mold and then degassed in a vacuum chamber (~1 mbar) for 4 min to avoid entrapped air in the epoxy. The epoxy was cured at room temperature for 24 h. The diameter and height of the epoxy micropillars were 200 and 400 μm, respectively. The pillars were hexagonally

[1]Corresponding author.

Contributed by the Applied Mechanics Division of ASME for publication in the Journal of Applied Mechanics. Manuscript received September 9, 2020; final manuscript received November 13, 2020; published online December 4, 2020. Assoc. Editor: Noy Cohen.

 Copyright © 2020 by ASME; reuse license CC-BY 4.0

Downloaded from http://asmedigitalcollection.asme.org/appliedmechanics/article-pdf/88/3/031009/6624807/jam_88_3_031009.pdf by Technische Informationsbibliothek (TIB) user on 05 July 2021

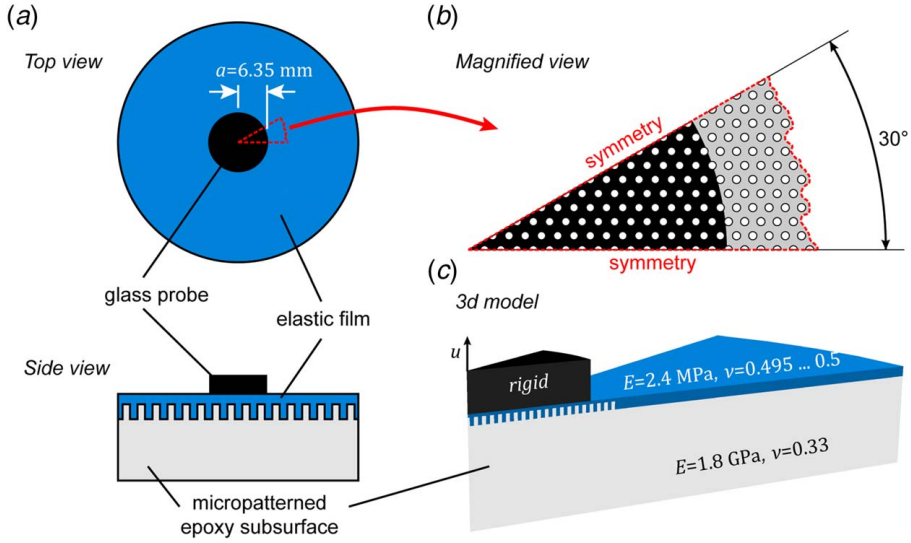

Fig. 1 Illustration of the problem and three-dimensional model for numerical simulations. (*a*) Top and side view of the glass probe (black) adhering to the center of the elastic film (blue). The elastic film covers the micropillar array (gray). (*b*) Inset showing 1/12th of the model and corresponding symmetry boundaries. (*c*) Three-dimensional model (1/12th) for numerical simulations, where micropillars located far away from the probe were ignored. Young's modulus, *E*, and Poisson's ratio, *ν*, of the elastic film and the micropatterned epoxy subsurface are given. The displacement of the rigid glass probe is *u*. (Color version online.)

arranged with a center-to-center distance of 400 μm. Next, a droplet of the liquid polydimethylsiloxane pre-polymer (PDMS, Sylgard 184, DOW Corning Corporation, Midland, USA) was placed onto a smooth silicon wafer. The two-component PDMS was mixed in a 10:1 ratio at 2350 rpm and degassed at 1 mbar for 3 min using a SpeedMixer. The cured epoxy array was pressed upside down into the droplet using various weights to adjust the thickness of the PDMS film. PDMS was cured at 95 °C in an oven for 2 h. After curing the adhesion of the film was tested as described later. Upon each adhesion test, an additional silicone layer was added to increase the thickness of the silicone film. To differentiate between various silicone layers, 5 wt% of blue and yellow pigments were alternately added to the PDMS pre-polymer during mixing. Silicone films with non-patterned epoxy subsurfaces were fabricated by following the same process described earlier using a non-patterned silicon wafer for epoxy replication. After all adhesion measurements, specimens were sectioned and thicknesses of the films were measured using optical microscopy.

2.2 Adhesion Tests. Adhesion tests were performed using a customized tensile tester (Inspekt table BLUE; Hegewald& Peschke, Nossen, Germany) equipped with a 50 N load cell. A nominal flat, smooth glass disc (Edmund optics, Barrington, New Jersey, USA) with a radius of 6.35 mm was used as a substrate (Fig. 1(*a*)). A mirror and a camera were mounted below the transparent glass substrate. The substrate was connected to a θ–ϕ goniometer (MOGO; Owis, Staufen im Breisgau, Germany) to align it with the specimen. The contact of the silicone film with the glass substrate was visualized by the principle of frustrated total internal reflection (frustrated TIR) as described previously in Refs. [12,13]. Contact formation and detachment were recorded using a digital camera (DMK 33GX236; Imaging Source Europe GmbH, Bremen, Germany) with a resolution of 1920 × 1080 pix and a frame rate of 50 fps. The specimens were brought in contact with the substrate with a velocity of 1 mm/min until the compressive preload of 20 N was achieved. The specimen was immediately retracted from the substrate in normal direction with an unloading rate of 1 mm/min. The highest tensile force during detachment

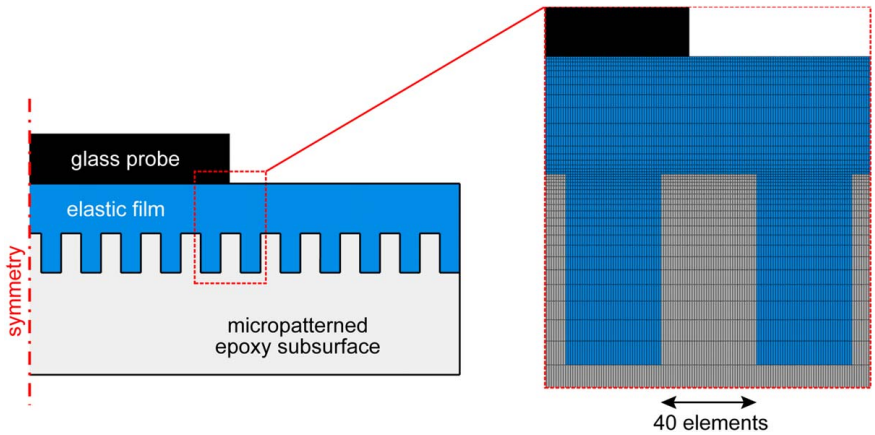

Fig. 2 Plane-strain model. Schematics of the plane-strain model showing a magnified region with the applied mesh.

Downloaded from http://asmedigitalcollection.asme.org/appliedmechanics/article-pdf/88/3/031009/6624807/jam_88_3_031009.pdf by Technische Informationsbibliothek (TIB) user on 05 July 2021

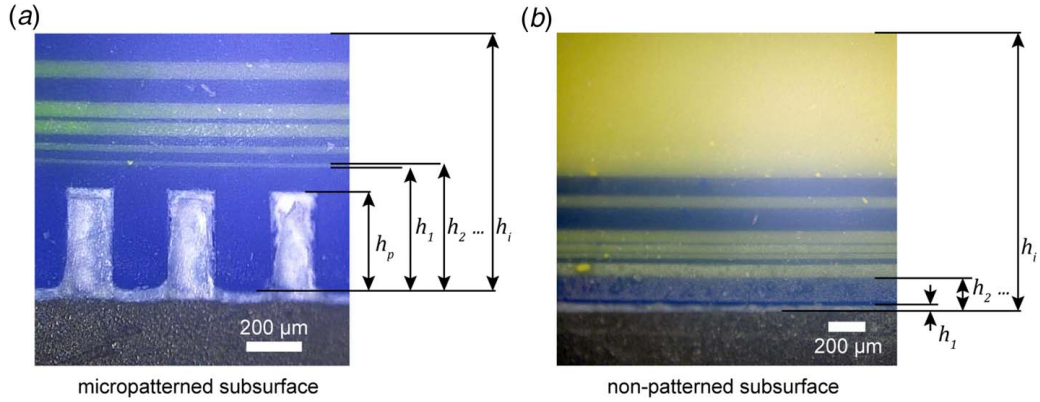

Fig. 3 Thicknesses of pigmented elastic films: (*a*) cross section of the specimen displaying dimensions of the micropatterned epoxy subsurface and the thickness of each layer h_i and (*b*) cross section of the specimen with the non-patterned subsurface

was defined as pull-off force, F_p. For each adhesion test, the mean value of two measurements at different locations was reported. To account for the elastic deformation of the testing device, the displacement of the glass substrate, u, was calculated as follows: $u = u_M - F/k$, where u_M is the displacement of the motorized stage, F is the force, and $k = 167$ kN/m is the machine stiffness.

IMAGEJ was used to analyze the recorded videos of the adhesion tests. Using this open-source software, videos recorded during the measurements were transformed into frames and binarized by choosing a threshold gray value, so as every pixel lower than that value was considered white (attached regions), whereas every pixel higher than that value was considered black (detached regions). Using "analyze particles tool," the number of cracks at the pull-off force was calculated. Edge cracks are defined as detachment along the perimeter, whereas cracks at the interior refer to cavities and cavitation. The smallest cavity radius that could be detected by the analyze particles tool was 50 μm. This value is related to the resolution of the images with pixel widths of about 30 μm.

3 Numerical Simulations

3.1 Calculation of the Stiffness and Effective Modulus. Three-dimensional (3D) numerical simulations were performed to determine the overall stiffness and the effective modulus for various values of h/a, where h is the film thickness and a is the radius of the glass disc. The three-dimensional model is illustrated in Fig. 1(*c*). Due to the hexagonal pattern of the micropillars, the geometry in the finite element (FE) model was simplified to 1/12th as shown in Fig. 1(*b*). The diameter and height of the epoxy micropillars were 0.2 and 0.4 mm, respectively. The center-to-center distance was 0.4 mm. The epoxy backing layer was 5 mm thick. The elastic modulus and the Poisson's ratio of the epoxy were 1.8 GPa and 0.33, respectively. The micropillars located far outside from the glass probe were ignored (Fig. 1(*c*)), as they have negligible effect on the stiffness of PDMS layer in contact with the probe. The elastic modulus of the PDMS was 2.4 MPa. The glass probe with a radius of 6.35 mm was set rigid. In the simulations, the Poisson's ratio and the height of the PDMS layer were varied. The FE calculations were performed using ABAQUS version 2019. The PDMS layer and the epoxy base were meshed with six-node linear triangular prism elements (C3D6) using mesh refinement beneath the glass probe. Each of them consisted of about 1.2 million elements. Hybrid elements were used for the PDMS layer. The bottom surface of the epoxy base was fixed, whereas ABAQUS' built-in cyclic symmetry feature was used to enforce the required symmetry condition. The loading was applied with prescribed vertical displacement of the top surface area of the glass probe. Linear static analyses were performed using small-strain formulation. The stored strain energy in the assembly was requested for each simulation. These values were used to calculate the stiffness by $k = 12 \cdot 2U_{12}/u^2$, where U_{12} represents the stored strain energy in the 1/12th model and u denotes the applied displacement. The normalized effective modulus was then calculated by $E_{eff}/E = hk/\pi a^2$, where a is the radius of the glass probe, E is the elastic modulus, and h is the thickness of the PDMS layer.

3.2 Interfacial Stress Distribution. The 3D FE models built for the stiffness calculations can be also used to extract the interfacial normal and shear stress distributions along the glass-PDMS interface. However, the analysis of the singularity domain along the perimeter of the probe would require a very fine 3D mesh with a small element size resulting in a FE model with an extensive number of elements. In order to reduce the corresponding computational cost, we proposed a simplified two-dimensional (2D) plane-strain model for the analysis of the stress distributions. The geometry of the plane-strain model is characterized by the same dimensions, namely a, h, the pillar height, and the pillar diameter. The material properties are the same as those used for the 3D

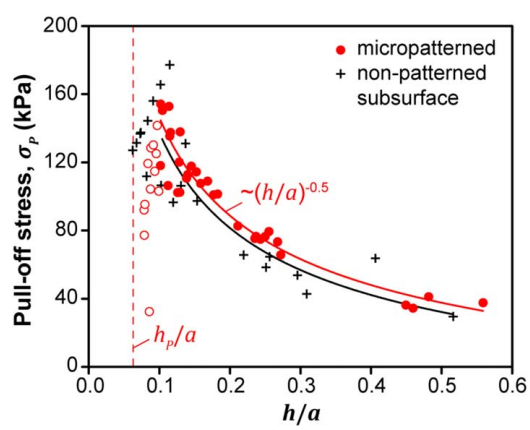

Fig. 4 Pull-off stress of silicone films in terms of confinement ratio *h/a*. Red circles and black crosses represent films with a micropatterned and a non-patterned subsurface, respectively. Red open circles display values for $h/a < 0.1$ of the films with micropatterned subsurface. These values were neglected in further analyses due to incomplete contacts of the very thin layers in the adhesion measurements (compare Appendix B). The vertical dashed line represents the height of the epoxy micropillars of 400 μm and $h/a = 0.063$. The solid red (micropatterned) and black (non-patterned) lines represent power fit functions $\sigma_P = A(h/a)^{-0.5} + B$, where *A* and *B* are constants. (Color version online.)

Downloaded from http://asmedigitalcollection.asme.org/appliedmechanics/article-pdf/88/3/031009/6624807/jam_88_3_031009.pdf by Technische Informationsbibliothek (TIB) user on 05 July 2021

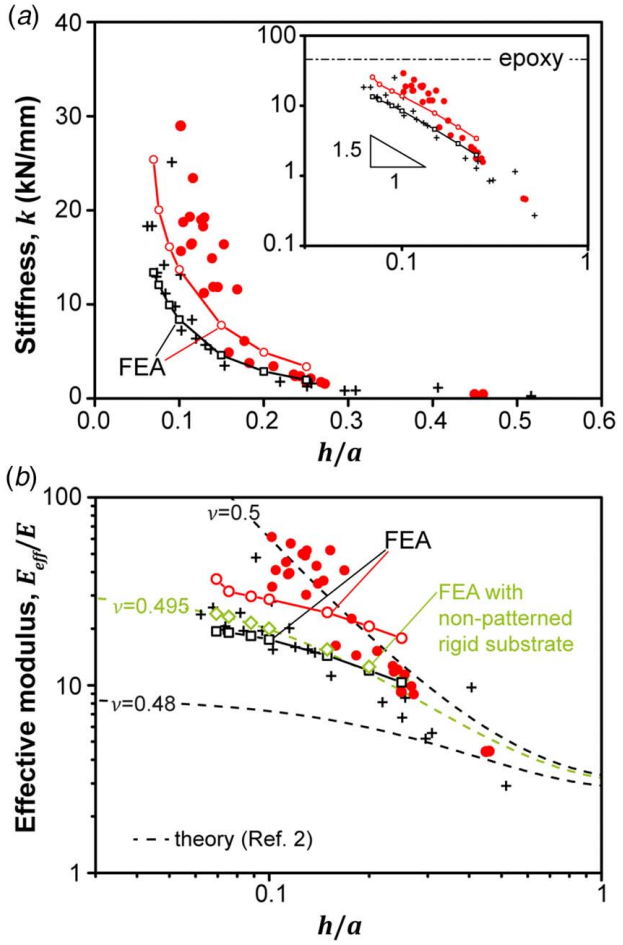

Fig. 5 Stiffness and normalized effective modulus in terms of the confinement ratio *h/a*. Red dots and black crosses represent experimental results of micropatterned and non-patterned subsurfaces, respectively. Empty red circles and empty black squares show numerical results of finite element analyses (FEA). In (*a*), the dashed-dotted line in the inserted log–log plot represents the stiffness of the non-patterned epoxy layer with an elastic modulus of 1.8 GPa and thickness of 5 mm. In (*b*), dashed lines are analytical solutions for a non-patterned rigid substrate and films with various Poisson's ratios reported in Ref. [2]. Green diamonds display numerical results for the non-patterned "rigid" subsurface layer with an elastic modulus of 1000 GPa. (Color version online.)

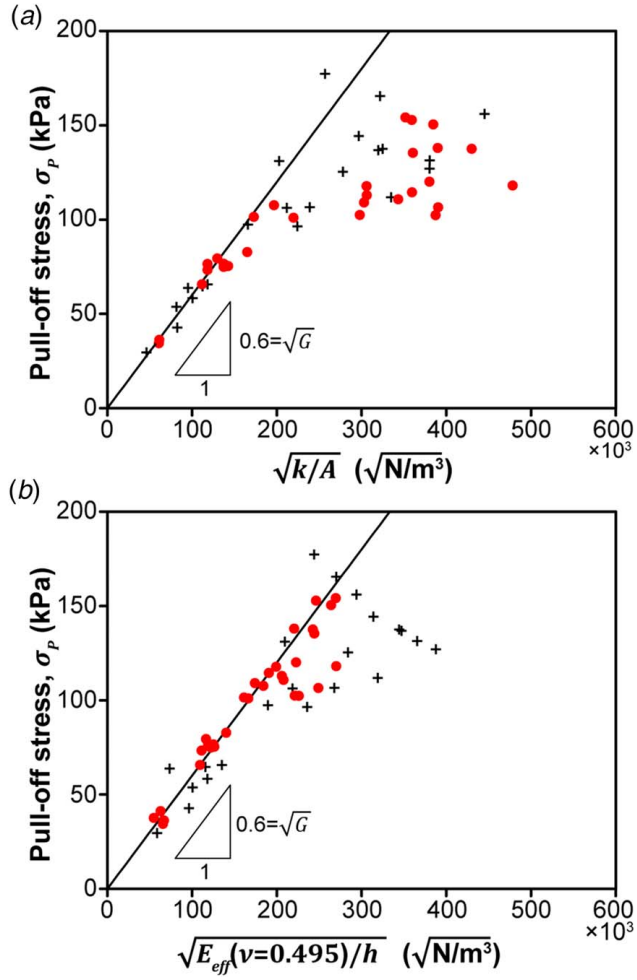

Fig. 6 Adhesion results in terms of scaling parameters. Red circles and black crosses represent films with micropatterned subsurface and films with non-patterned subsurface, respectively. (*a*) Pull-off stress in terms of $\sqrt{k/A}$ that assumes incompressible films with a Poisson's ratio of 0.5 [3]. (*b*) Pull-off stress in terms of $\sqrt{E_{eff}/h}$ as described by Eq. (2), where E_{eff} was calculated for $\nu = 0.495$ (see Appendix C). The slope of the linear function in both plots equals $\sqrt{G}$, where *G* is the energy release rate. (Color version online.)

simulations. The bottom surface of the epoxy base is fixed, whereas the movement of the rigid glass probe is modeled with prescribed vertical displacement along the interface. Only a half-model is used due to the symmetry of the assembly. The schematics of the model geometry are depicted in Fig. 2, where the density of the applied mesh is also shown for a particular set of geometrical parameters.

The proposed model allowed us to use a large number of elements along the interface. Each pillar contains 40 elements along the radial direction. Four-node bilinear plane strain quadrilateral elements are used in the model with a full integration scheme. The hybrid formulation is adopted for the elastic layer due to the high value of the Poisson's ratio. The following model parameters were varied in the analyses: Poisson's ratio, the height of the elastic layer (h), the height of the pillars, and radius of the probe. Our assumption is that the simplified plane-strain model can be used to analyze the characteristics of the stress distributions and their dependencies on the model parameters. It is expected that the conclusions based on the results of the plane-strain model can be generalized to the three-dimensional model.

4 Results and Discussion

Figure 3 displays cross sections of the silicone films (PDMS) with a micropatterned (Fig. 3(*a*)) and a non-patterned (Fig. 3(*b*)) epoxy subsurface that was successfully manufactured by replica molding. After the first PDMS layer with the thickness h_1 was deposited, an adhesion test was performed. An additional PDMS layer was added after this measurement to increase the thickness of the silicone film, h_2. Subsequently, the adhesion was measured again. Consecutive PDMS layers contained alternating blue and yellow pigments. Using this method, the thickness of each layer of the sample could be determined after all adhesion tests (Fig. 3). Moreover, pigments acted as scattering centers during the frustrated total reflection, which enabled the visualization of the actual contact area during the attachment and detachment [12]. The elastic moduli of the silicone films containing 5% blue or yellow pigments were similar to the elastic modulus of the transparent PDMS, which was 2.4 MPa (see Fig. 10 in Appendix A).

Figure 4 displays the results of the adhesion tests in terms of the confinement ratio h/a, where h is the thickness of the silicone film (as defined in Fig. 3) and a is the radius of the glass disc adhering to the film. For patterned and non-patterned subsurfaces, pull-off

Downloaded from http://asmedigitalcollection.asme.org/appliedmechanics/article-pdf/88/3/031009/6624807/jam_88_3_031009.pdf by Technische Informationsbibliothek (TIB) user on 05 July 2021

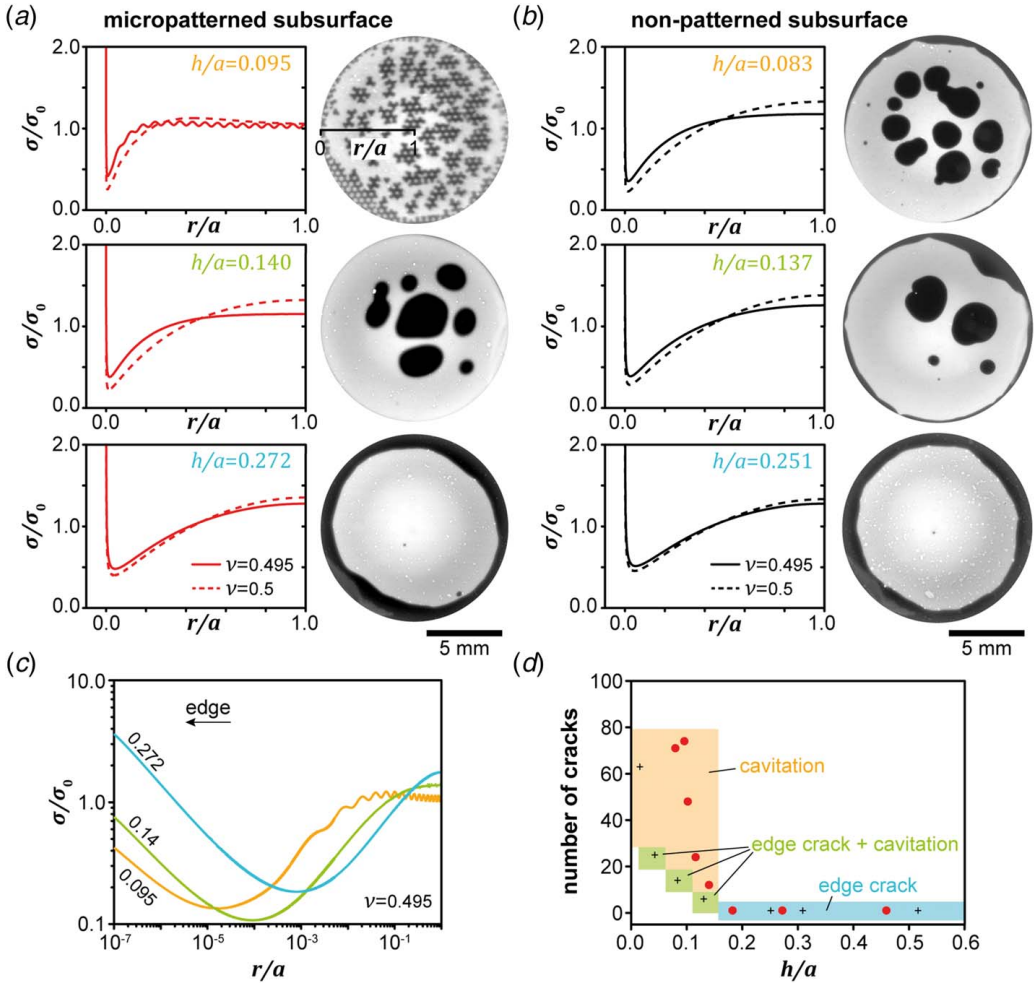

Fig. 7 Interfacial stress distribution and detachment. (*a*,*b*) Numerical plane strain results of the stress distribution normalized by the average normal stress (left half of the contact) and corresponding images at pull-off (right). Solid lines represent results for $\nu = 0.495$ and dashed lines for $\nu = 0.5$ (the exact value is 0.4999999, the maximum value, which is used by ABAQUS). (*a*) Micropatterned subsurface with $h/a = 0.095$, $h/a = 0.140$, and $h/a = 0.272$. (*b*) Non-patterned subsurface with $h/a = 0.083$, $h/a = 0.137$, and $h/a = 0.251$. (*c*) Log–log plot of the stress distribution for micropatterned subsurface shown in (*a*) for $\nu = 0.495$. (*d*) Number of cracks in terms of the confinement ratio h/a and classification of the detachment mechanisms for the micropatterned (red dots) and non-patterned (black crosses) subsurface. (Color version online.)

stresses, σ_P, were maximum at $h/a \approx 0.1$, at which the maximum pull-off stresses were 154 and 177 kPa for the micropatterned and the non-patterned subsurfaces, respectively. With increasing h/a, the pull-off stresses decayed to a quarter of the peak values with a scaling of $(h/a)^{-0.5}$, as indicated by the fit functions (solid lines) in Fig. 4. The fit functions revealed slightly higher adhesion for the films with micropatterned subsurface compared to the non-patterned one. Lower adhesion values for $h/a < 0.1$ were attributed to incomplete contacts during the attachment due to uneven surfaces of the very thin silicone films (see Fig. 11 in Appendix B). In fact, very thin films shrunk in the area between adjacent microcolumns during curing, resulting in a surface waviness similar to the micropattern. Furthermore, thin films were more sensitive to misalignment, which is even more severe for the films with micropatterned subsurfaces. For the analyses presented below, we neglected data for $h/a < 0.1$ due to incomplete contacts (open circles in Fig. 4).

Figure 5 depicts the stiffness, k and the effective modulus, E_{eff} of the films in terms of the confinement ratio, h/a. The stiffness was determined from individual force-displacement curves in the compressive, linear regime during retraction. With decreasing h/a, the stiffness of the films exponentially increased over two orders of magnitude from 0.27 to 30 kN/mm (Fig. 5(*a*)). The increase in stiffness is caused by the restricted lateral contraction of the silicone films due to confinement [2]. The values were below the stiffness of 45 kN/mm, which is the upper bound corresponding to the non-patterned epoxy film with a thickness of 5 mm and an elastic modulus of 1.8 GPa (see inset in Fig. 5(*a*)). The numerically results of the stiffness (empty circles) scaled with $(h/a)^{-1.5}$ for both subsurfaces, where the stiffness with micropatterned subsurface was about 1.7 times higher compared to the non-patterned subsurface. The numerical results were in good agreement with the experimental results obtained for the non-patterned subsurface. For the micropatterned subsurface, however, numerical results underestimated the stiffnesses obtained from experiments for small h/a. The deviation is probably related to the fact that the elastic deformation of the micropatterned epoxy subsurface was included in the numerical analysis, but ignored in the experiments.

Similar trends were observed for the normalized effective modulus, E_{eff}/E, as it was calculated from the stiffness as follows:

$$E_{eff}/E = \frac{hk}{\pi a^2} \tag{1}$$

where E is the intrinsic elastic modulus of the films of 2.4 MPa (Fig. 5(*b*)). With increasing confinement, i.e., decreasing h/a, the

Downloaded from http://asmedigitalcollection.asme.org/appliedmechanics/article-pdf/88/3/031009/6624807/jam_88_3_031009.pdf by Technische Informationsbibliothek (TIB) user on 05 July 2021

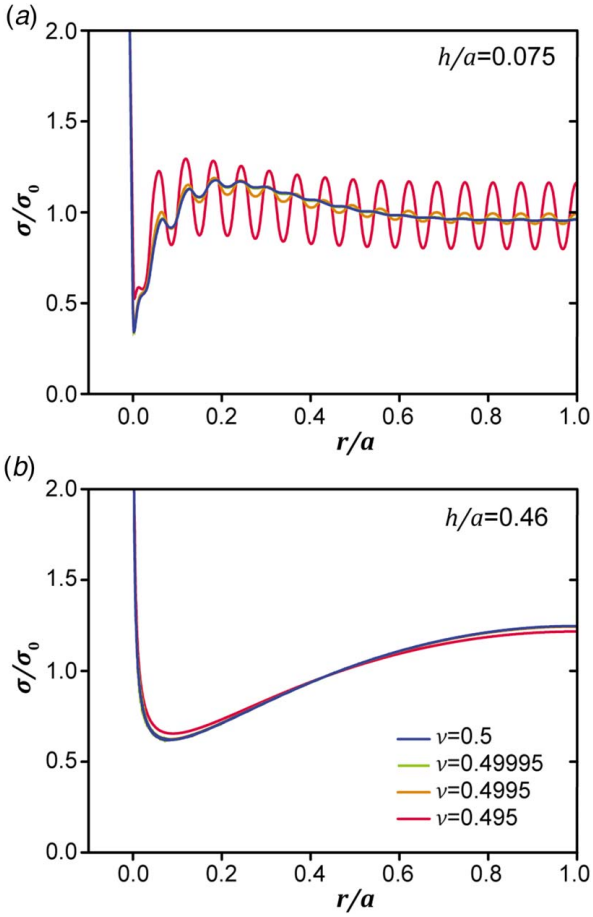

Fig. 8 Effect of Poisson's ratio. Numerical plane strain results of the interfacial stress distribution normalized by the average normal stress for (*a*) $h/a = 0.075$ and (*b*) $h/a = 0.46$. (Color version online.)

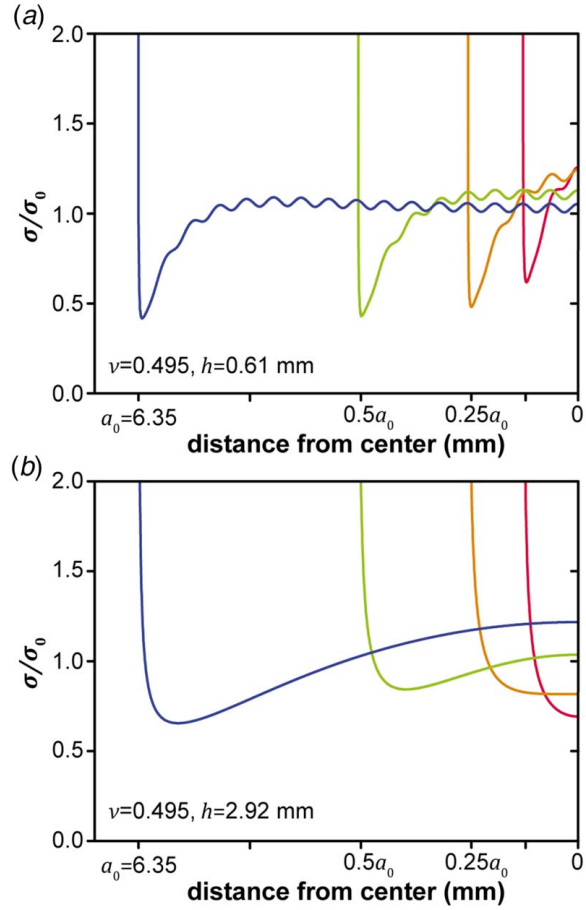

Fig. 9 Effect of the radius of the glass disc. Numerical plane strain results of the interfacial stress distribution normalized by the average normal stress for (*a*) $h = 0.61$ mm and (*b*) $h = 2.92$ mm. The Poisson's ratio was 0.495. (Color version online.)

effective modulus increased from 3 (i.e., the lower limit of unconfined films [2]) to 26 for the films with non-patterned and up to 61 for the films with micropatterned subsurfaces. This trend was not reproduced by the numerical simulations, where the ratio of the effective moduli of films with micropatterned subsurfaces to films with non-patterned subsurfaces was again about 1.7. In addition to experimental and numerical results, Fig. 5(*b*) displays analytical solutions for films with non-patterned, rigid subsurfaces (dashed lines), as reported in Ref. [2]. These results largely vary with the Poisson's ratio. For example for $h/a = 0.1$, the modulus is one order of magnitude larger for a Poisson's ratio of 0.5 compared to 0.48. Experimental values (black crosses) and numerical simulations matched with the analytical solution for $\nu = 0.495$ (green dashed line). The result implies that the Poisson's ratio of the silicone films was 0.495, which is in accordance with the Poisson's ratio of Sylgard 184 measured by thermal expansion and an optical surface profilometry [5]. It should be noted that the numerical results (black squares) slightly underestimated the theoretical values, because of the elasticity of the epoxy subsurface. An additional simulation with a much larger Young's modulus of 1000 GPa (green diamonds) agrees with the theoretical model.

The trend of the effective elastic moduli obtained from experiments with the micropatterned subsurface follows the theory for $\nu = 0.5$. This result may suggest that the lateral contraction of the film is additionally limited by the presence of the embedded microstructures. However, simulations (open red circles in Fig. 5(*b*)) could not confirm this observation, as it was similar to that obtained for the non-patterned subsurface. Thus, the higher moduli were likely caused by experimental issues such as the uneven surfaces of very thin silicone films (Fig. 11 in Appendix B) and the higher sensitivity to misalignment compared to the non-patterned subsurface, as the embedded micropillars reduced the compliance of the film.

Recently, Bartlett et al. proposed a scaling model that brings the pull-off stress into a linear relationship with $\sqrt{k/A}$ [3]. Figure 6(*a*) displays our experimental results with and without a micropatterned subsurface. Below $200 \cdot 10^3 \sqrt{\mathrm{N/m^3}}$, the pull-off force scaled linearly with a slope of 0.6, which is equal to $\sqrt{G}$; thus, the energy release rate $G = 0.36\ \mathrm{J/m^2}$. Above $200 \cdot 10^3\ \sqrt{\mathrm{N/m^3}}$, the data scattered strongly and were below the prediction. An explanation for that deviation could be the restriction of the model to incompressible materials, i.e., $\nu = 0.5$. However, as shown in Fig. 5, slight compressibility of the material ($\nu < 0.5$) leads to a drastic reduction of the stiffness and the effective elastic modulus for large confinements. To account for that, the scaling parameter was corrected by considering the effective elastic modulus, being a function of the confinement ratio h/a and the Poisson's ratio ν (see Appendix C). Hence, the pull-off stress scales as follows:

$$\sigma_p \sim \sqrt{G}\sqrt{\frac{E_{eff}}{E}\left(\frac{h}{a}, \nu\right)\frac{E}{h}} = \sqrt{G}\sqrt{\frac{E_{eff}}{h}} \tag{2}$$

where $E_{eff}/E(h/a, \nu)$ is the effective modulus in terms of h/a and ν, which refers to Eq. (C4) in Appendix C. Figure 6(*b*) displays the pull-off stress as a function of the corrected scaling argument $\sqrt{E_{eff}/h}$ for $\nu = 0.495$. Now, the experiments follow the linear trend with reduced scattering compared to Fig. 6(*a*). The slope again relates to the energy release rate of $G = 0.36\ \mathrm{J/m^2}$.

Downloaded from http://asmedigitalcollection.asme.org/appliedmechanics/article-pdf/88/3/031009/6624807/jam_88_3_031009.pdf by Technische Informationsbibliothek (TIB) user on 05 July 2021

In the pull-off experiments, we observed various detachment mechanisms such as edge cracks and cavitation. Edge cracks propagated radially from the circumference of the glass disc toward the center of the contact. Cavitation occurred at the contact area, where cracks propagated from inside toward the edge of the disc and, therefore, in opposite direction to edge cracks. It should be noted that cavitation occurred at different locations simultaneously and that cavities coalesce as they grow. In contrast, an edge crack exhibited only a single crack front. The detachment behavior obtained was compared to plane strain simulations of the interfacial stress distribution, as depicted in Fig. 7 and Figs. 12 and 13 in Appendix D. Stress distributions varied in terms of confinement (h/a), the Poisson's ratio, and the subsurface microstructure. The latter diminishes for thicker films, as for example shown for $h/a \approx 0.25$, at which the film thickness is four times the pillar height. The stress distribution and the detachment via edge cracks were similar for the micro and the non-patterned subsurface. For thinner films, a transition from edge cracks to cavitation was observed, whereas a mixed mode of cavitation and edge cracks was found for the non-patterned subsurface. As depicted in Fig. 7(*c*), the transition from edge cracks to cavitation refers to the reduction of the magnitude of the intensity of the edge singularity by one order of magnitude, although the center stress simultaneously decreased by less than a factor of two. The interfacial stress distribution was almost constant for $r/a \geq 0.2$ for the thinnest film ($h/a = 0.095$) with the micropatterned subsurface. Due to the slight compressibility of the film ($\nu = 0.495$), the stress distribution was wavy, which indicates the underlying micropattern, and explains cavitation along the entire interface. The detachment regimes and the number of corresponding cracks recorded at pull-off are summarized in Fig. 7(*d*).

Plane strain simulations further provide insight into the effect of the Poisson's ratio (Fig. 8) and the size of the glass disc (Fig. 9) on the interfacial stress distribution (all data are available online, see Supporting Data). The overall distributions along the interface were similar for different Poisson's ratios, but the more compressible the material, the more dominant the wavy character, which could induce cavitation atop the embedded micropillars (Fig. 8(*a*)). The effect of the Poisson's ratio diminishes with increasing h/a, as shown in Fig. 8(*b*). The variation of the radius of the glass disc has influence on the confinement ratio, h/a (Fig. 9). Figure 9(*a*) shows that although the confinement ratio decreases with smaller radii of the discs, the wavy shape of the stress distribution remains for a constant film thickness of $h = 0.61$ mm. Figure 9(*b*) shows a film with $h = 2.92$ mm, where the stress distribution reflects the transition from a confined film for $a_0 = 6.35$ mm (blue line) to an unconfined film for $0.125\ a_0 = 0.79$ mm (red line).

5 Conclusions

A micropatterned subsurface was introduced into highly confined elastic films. The following conclusions can be drawn:

- Adhesion scales with the confinement ratio $(h/a)^{-0.5}$; however, the embedded micropattern only slightly improved the adhesion performance.
- The stiffness of the adhesives scales with $(h/a)^{-1.5}$, whereas the micropatterned subsurface enhanced the stiffness due to the presence of the embedded micropillars. Similar trends were obtained for the effective modulus. Comparing experimental and numerical results with the theoretical prediction led to the conclusion that the silicone films were slightly compressible with a Poisson's ratio of 0.495.
- Adhesion results were compared with the scaling argument $\sqrt{k/A}$, which was then modified to $\sqrt{E_{eff}/h}$ to account for compressible materials, as E_{eff} varies with ν. Based on that, the energy release rate of 0.36 J/m^2 was determined for both subsurfaces, indicating that adhesion is insensitive to the presence of the microstructures.
- Interfacial stress distributions obtained from finite element simulations were compared to images taken at pull-off to explain the transition from edge cracks (unconfined films) to cavitation (confined films). Compressibility of the elastic layer introduced a wavy stress distribution that, in turn, introduced a higher amount of cavities atop the embedded micropillars.

Acknowledgment

M. S. and R. H. acknowledge funding by the Leibniz Competition Grant No. K279/2019. A. K. acknowledges support by the UNKP-19-3 New National Excellence Program of the Ministry for Innovation and Technology, Hungary and by the Hungarian National Research, Development and Innovation Office (NKFI FK 128662).

Conflict of Interest

There are no conflicts of interest.

Data Availability Statement

The datasets generated and supporting the findings of this article are obtainable from the corresponding author upon reasonable request. The data and information that support the findings of this article are freely available online.[2] The authors attest that all data for this study are included in the paper.

Supporting Data

All data are available online.[3]

Appendix A: Storage Modulus of Silicone Films

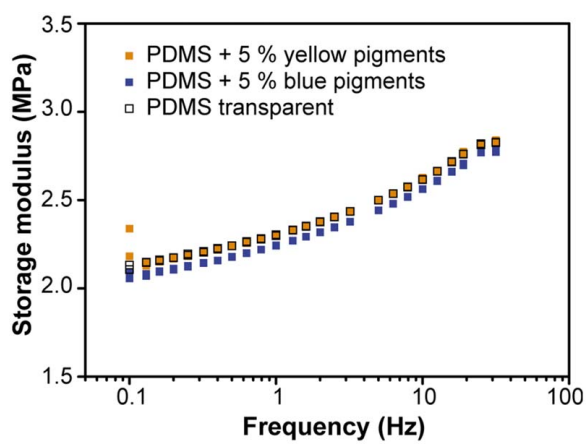

Fig. 10 Storage modulus of silicone (PDMS) films with 5% blue (blue squares) or yellow (yellow squares) pigments in comparison to a silicon film without pigments (open black boxes) (Color version online.)

[2]https://www.researchgate.net/publication/345806240_Effect_of_subsurface_microstructures_on_adhesion_of_highly_confined_elastic_films

[3]See Note 2.

Downloaded from http://asmedigitalcollection.asme.org/appliedmechanics/article-pdf/88/3/031009/6624807/jam_88_3_031009.pdf by Technische Informationsbibliothek (TIB) user on 05 July 2021

Appendix B: Surface Characterization of Elastic Films

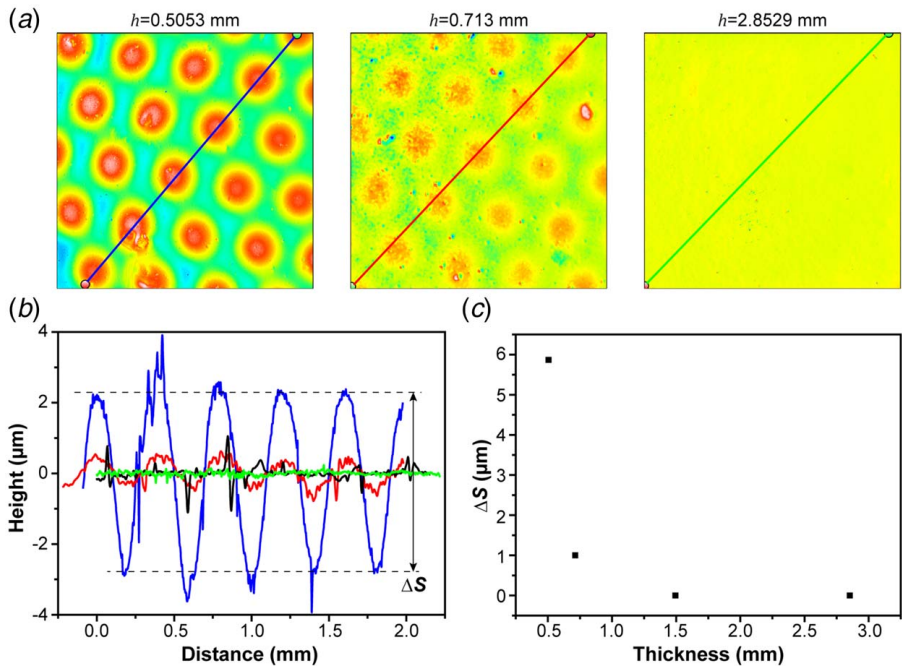

Fig. 11 Surface scans of elastic films: (*a*) confocal microscope scans of 1.6 × 1.6 mm^2 of various thick films with micropatterned subsurfaces. Lines indicate the position of height scans shown in (*b*), at which blue refers to $h = 0.5053$ mm, red to $h = 0.713$ mm, black to $h = 1.494$ mm, and green to $h = 2.8529$ mm. (c) Mean peak-to-valley distance, ΔS in terms of film thickness. (Color version online.)

Appendix C: Scaling Argument for Slightly Compressible Films

We consider an adhesive bond between a smooth elastic film and a rigid, nominal flat disc that is normally loaded with a force F. The contact separates at a critical force F_p, at which the elastic strain energy stored at the interface is primarily recovered by breaking bonds and forming new surface. Viscoelastic effects were ignored. The critical force can be calculated as follows [3]:

$$F_p \sim \sqrt{G}\sqrt{Ak} \tag{C1}$$

where G is the energy release rate, A is the contact area, and k is the stiffness of the film. Note that k varies with the confinement ratio h/a, where h is the film thickness and a is the radius of the rigid disc in contact with the film.

The pull-off stress σ_p is the critical force divided by the contact area. Thus, Eq. (C1) can be rewritten as:

$$\sigma_p = \sqrt{G}\sqrt{\frac{k}{A}} \tag{C2}$$

With $k = \Delta F/\Delta u$, where Δu is the relative displacement of the disc normally to the adhesive interface, Eq. (C2) gives:

$$\sigma_p = \sqrt{G}\sqrt{\frac{\Delta F}{A}\frac{1}{\Delta u}} = \sqrt{G}\sqrt{\frac{\Delta\sigma}{\Delta\varepsilon}\frac{1}{h}} = \sqrt{G}\sqrt{\frac{E_{eff}}{h}} \tag{C3}$$

where E_{eff} is the effective elastic modulus that similar to k varies with the confinement ratio h/a.

As previously reported, the E_{eff} of confined films is sensitive to the Poisson's ratio ν and h/a [2]. For $0.48 \le \nu \le 0.5$, the normalized effective elastic modulus is given by

$$\frac{E_{eff}}{E}\left(\frac{h}{a}, \nu\right) = \frac{K_1 + h/a}{K_2 + (h/a)^{K_3}} + \frac{K_4 + h/a}{K_5 + (h/a)^{K_6}} \tag{C4}$$

where E is the intrinsic elastic modulus and the parameters K_i ($i = 1, \ldots, 6$) are functions of Poisson's ratio as follows:

$$\begin{aligned}
K_1 &= 0.1811 - 33.6939\,(0.5-\nu)^{0.715} + 5.2574\nu \\
K_2 &= -3.531 + 2.3473(0.5-\nu)^{0.5256} + 9.2434\nu \\
K_3 &= -30.12 - 0.4099\,(0.5-\nu)^{0.2384} + 59.1455\nu \\
K_4 &= 14.5412 + 3.8871(0.5-\nu)^{0.5213} - 28.0909\nu \\
K_5 &= 2.266 + 199.591(0.5-\nu)^{1.9625} - 4.5322\nu \\
K_6 &= 21.5731 - 25.3997(0.5-\nu)^{0.7325} - 39.1534\nu
\end{aligned} \tag{C5}$$

Downloaded from http://asmedigitalcollection.asme.org/appliedmechanics/article-pdf/88/3/031009/6624807/jam_88_3_031009.pdf by Technische Informationsbibliothek (TIB) user on 05 July 2021

Appendix D: Contact Images at Adhesive Failure of the Contact

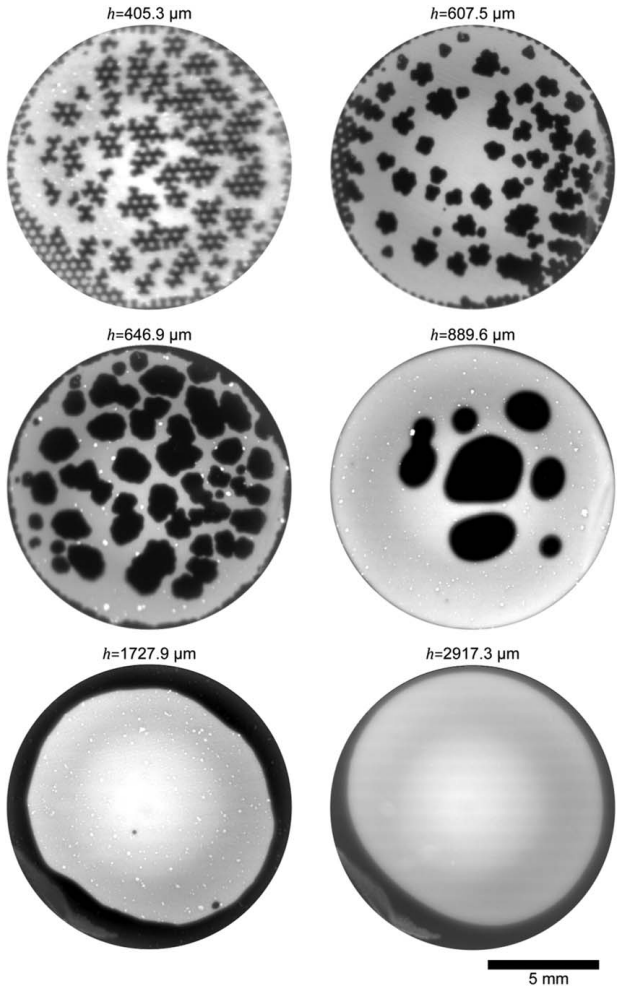

Fig. 12 Contact images at pull-off of films with micropatterned subsurface

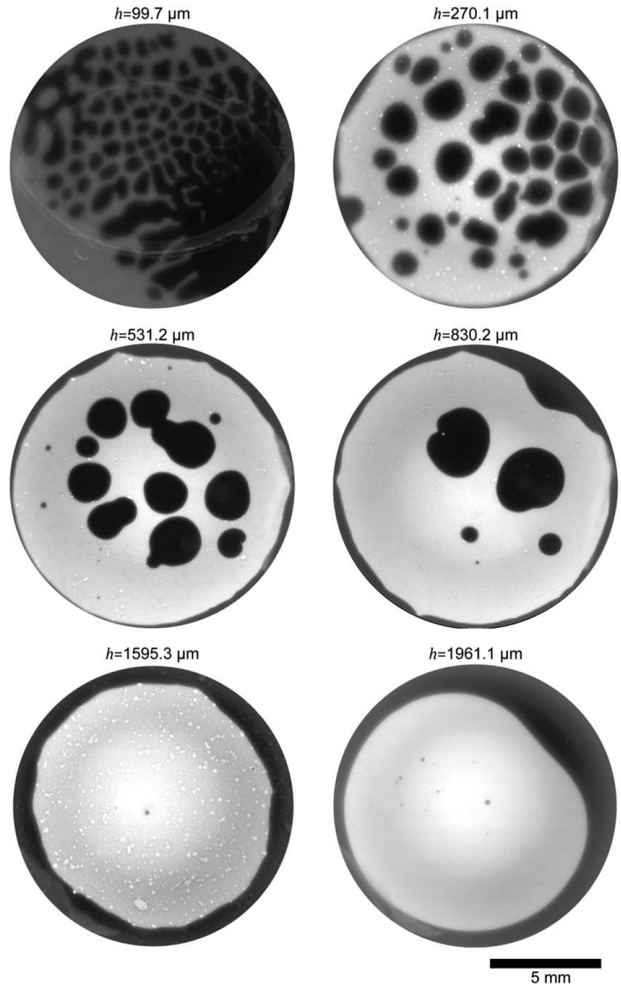

Fig. 13 Contact images at pull-off of films with non-patterned subsurface

References

[1] Kendall, K., 1971, "The Adhesion and Surface Energy of Elastic Solids," J. Phys. D. Appl. Phys., **4**(8), pp. 1186–1195.

[2] Hensel, R., McMeeking, R. M., and Kossa, A., 2019, "Adhesion of a Rigid Punch to a Confined Elastic Layer Revisited," J. Adhes., **25**(1), pp. 44–63.

[3] Bartlett, M. D., and Crosby, A. J., 2013, "Scaling Normal Adhesion Force Capacity With a Generalized Parameter," Langmuir, **29**(35), pp. 11022–11027.

[4] Lindsey, G. H., 1967, "Triaxial Fracture Studies," J. Appl. Phys., **38**(12), pp. 4843–4852.

[5] Müller, A., Wapler, M. C., and Wallrabe, U., 2019, "A Quick and Accurate Method to Determine the Poisson's Ratio and the Coefficient of Thermal Expansion of PDMS," Soft Matter, **15**(4), pp. 779–784.

[6] Ganghoffer, J. F., and Gent, N., 1995, "Adhesion of a Rigid Punch to a Thin Elastic Layer," J. Adhes., **48**(1–4), pp. 75–84.

[7] Balijepalli, R. G., Fischer, S. C. L., Hensel, R., McMeeking, R. M., and Arzt, E., 2017, "Numerical Study of Adhesion Enhancement by Composite Fibrils With Soft Tip Layers," J. Mech. Phys. Solids, **99**, pp. 357–378.

[8] Creton, C., and Lakrout, H., 2000, "Micromechanics of Flat-Probe Adhesion Tests of Soft Viscoelastic Polymer Films," J. Polym. Sci., Part B: Polym. Phys., **38**(7), pp. 965–979.

[9] Shull, K. R., and Creton, C., 2004, "Deformation Behavior of Thin, Compliant Layers Under Tensile Loading Conditions," J. Polym. Sci., Part B: Polym. Phys., **42**(22), pp. 4023–4043.

[10] Crosby, A. J., Shull, K. R., Lakrout, H., and Creton, C., 2000, "Deformation and Failure Modes of Adhesively Bonded Elastic Layers," J. Appl. Phys., **88**(5), pp. 2956–2966.

[11] Fischer, S. C. L., Arzt, E., and Hensel, R., 2017, "Composite Pillars With a Tunable Interface for Adhesion to Rough Substrates," ACS Appl. Mater. Interfaces, **9**(1), pp. 1036–1044.

[12] Tinnemann, V., Hernández, L., Fischer, S. C. L., Arzt, E., Bennewitz, R., and Hensel, R., 2019, "In Situ Observation Reveals Local Detachment Mechanisms and Suction Effects in Micropatterned Adhesives," Adv. Funct. Mater., **29**(14), p. 1807713.

[13] Thiemecke, J., and Hensel, R., 2020, "Contact Aging Enhances Adhesion of Micropatterned Silicone Adhesives to Glass Substrates," Adv. Funct. Mater., p. 2005826.

Downloaded from http://asmedigitalcollection.asme.org/appliedmechanics/article-pdf/88/3/031009/6624807/jam_88_3_031009.pdf by Technische Informationsbibliothek (TIB) user on 05 July 2021